DD

JET–P(98)02

L C Ingesson et al

Soft X-ray Tomography during ELMs and Impurity Injection in JET

CERN LIBRARIES, GENEVA
SCAN-9807084

sw9829

JOINT EUROPEAN TORUS

This document is intended for publication in the open literature. It is made available on the understanding that it may not be further circulated and extracts or references may not be published prior to publication of the original, without the consent of the Publications Officer, JET Joint Undertaking, Abingdon, Oxon, OX14 3EA, UK.

Enquiries about Copyright and reproduction should be addressed to the Publications Officer, JET Joint Undertaking, Abingdon, Oxon, OX14 3EA, UK.

JET–P(98)02

Soft X-ray Tomography during ELMs and Impurity Injection in JET

L C Ingesson, B Alper, H Chen[1], A W Edwards, G C Fehmers[2], J C Fuchs[3], R Giannella[4], R D Gill, L Lauro-Taroni, M Romanelli[1].

JET Joint Undertaking, Abingdon, Oxfordshire, OX14 3EA,
[1]Also at Imperial College, London, SW7 2BZ, UK.
[2] Technische Universiteit Eindhoven, P O Box 513, 5600 MB Eindhoven, The Netherlands.
Present Address: Shell Research, Rijswijk, The Netherlands.
[3] Max-Planck-Institut für Plasmaphysik, EURATOM-Association, D-85748, Garching, Germany.
[4] Present Address: CEA Cadarache, F-13108 St. Paul-lez-Durance, France.

Preprint of a Paper to be submitted for publication in Nuclear Fusion

January 1998

ABSTRACT

The soft x-ray diagnostic at JET views the plasma from six directions with a total of 215 lines of sight. The good coverage of the plasma makes it possible to make detailed tomographic reconstructions of the soft x-ray emission during various conditions. We discuss one of the tomography methods applied at JET: a grid-based constrained optimization method that uses anisotropic smoothness on flux surfaces as regularization. This method has made it possible to study in detail the transport of heavy trace impurities injected into the plasma by laser blow-off. Impurity injection experiments in hot-ion H mode and optimized-shear plasmas are presented and discussed. The addition of a number of features to the algorithm, notably a non-negativity constraint, has made it possible to reconstruct very localized soft x-ray emission from the wall during ELMs. The detectors suffer damage from the neutrons produced in DD fusion reactions. This damage influences the sensitivity of the detectors, which makes it necessary to cross-calibrate the cameras. A method based on tomographic reconstructions has been developed to achieve the cross-calibration.

PACS numbers: 52.70.La, 42.30.Wb, 52.25.Vy, 52.25.Fi, 52.25Nr

1. INTRODUCTION

Soft x-ray (SXR) tomography is an important tool to study various phenomena in fusion plasmas. The technique was pioneered by groups in several laboratories using one camera and making use of plasma rotation [1–4]. Full tomography with at least two cameras was realised soon afterwards [5–7]. Later, systems with 5 to 7 cameras were developed [8–13]. The technique has been used to study a variety of phenomena, such as sawteeth (see e.g. Refs. 14–16), MHD events such as snakes [17], pellet enhanced performance modes [18] and disruptions. Furthermore, impurity injection studies have been carried out in the SXR range for a long time, and have also been carried out with the help of SXR tomography. In the past the impurity injection method to study particle transport has been applied to Ohmic, L mode [19,20] and H-mode plasmas [21]. Together with improvements in the analysis method, the current JET SXR system and processing make it possible to achieve unprecedented resolution, detail and accuracy, which makes more detailed transport studies possible than before.

In the past, the main tomographic reconstruction technique applied to soft x-ray tomography was the Cormack method [7], which has sometimes been applied in the magnetic flux geometry [22]. Other methods are algorithms similar to the Algebraic Reconstruction Technique [23,24], Maximum Entropy methods [25,26], and constrained optimization methods [27]. Recently, algorithms in flux coordinates to specifically pick out MHD modes have been developed [28,29]. The Cormack method was a good choice in some applications for systems with only a few cameras, although it can be applied successfully to multi-camera systems as well [11].

However, in many cases it is too restrictive. To take full advantage of the available information in modern multi-camera systems, there is a shift to more flexible algorithms, such as the constrained optimization method discussed in this paper.

The first aim of this paper is to discuss the constrained optimization method with which excellent reconstructions are obtained of the SXR emission in JET. The method is based on an algorithm that has been applied to bolometer tomography at ASDEX-Upgrade [30] and at JET [31], and SXR tomography at ASDEX-Upgrade [13]. Features and extensions included in the algorithm presented here are: anisotropic smoothness on flux surfaces, a non-negativity constraint, basis functions that describe an interpolation between grid points, and taking into account the full geometric properties of the detection system. In this paper the high spatial resolution that can be obtained in combination with the 215-channel SXR system on JET is demonstrated. The second aim is to discuss results of the study of transport by means of impurity injection in hot-ion H mode and optimized-shear plasmas, and results on SXR emission from the wall during Edge Localized Modes (ELMs). The reconstructions are much better than has been achieved before with a two-camera system on JET.

The 215-channels SXR diagnostic has been operational on JET since 1995. Technical details have been published elsewhere [11]. The diagnostic consists of 11 cooled miniature diode arrays mounted in-vessel in one poloidal cross-section. Each array views the plasma through an aperture. Ten of the arrays, with 18 channels each, are grouped in pairs to give nearly complete fan-views of the plasma (Fig. 1), whereas the array viewing vertically has 35 channels. Each nearly complete view we call "camera." An additional camera identical to the vertical camera is located in another poloidal cross-section to study toroidal asymmetries; however, it is not used for the tomographic reconstructions. In 1996, the upper array of camera EF (see Fig. 1) was replaced by a windowless system viewing the divertor, and was therefore not available for the tomographic reconstructions of some of the cases discussed in this paper. Technical aspects directly relevant for this paper that are discussed in detail are: (a) neutron damage to the

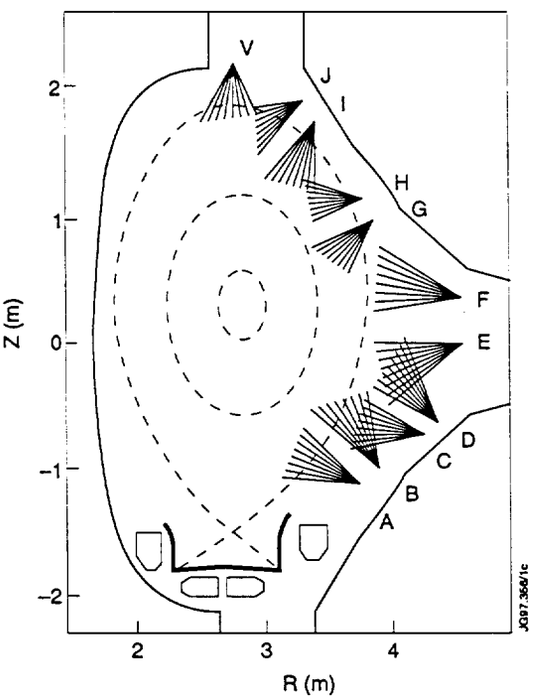

FIG. 1 Lay-out of the lines of sight of the JET SXR tomography system (not all shown). Ten of the detector arrays (each with 18 lines of sight), designated by A ... J, are grouped in pairs; each pair giving nearly complete views of the plasma. The single vertical array is designated camera V (35 lines of sight).

detectors, (b) the accuracy of positioning of the cameras, (c) the beam widths of the detection system, and (d) the Be filter. (a) Neutrons produced by DD fusion reactions in the plasma damage the detectors, thus influencing their sensitivity. Because the damage is different for different detectors, a method had to be developed to cross-calibrate the detectors in-vessel. (b) A considerable effort has been made to determine the positions and viewing directions of the detectors because these have to be known accurately to be able to carry out tomographic reconstructions. (c) To collect a sufficient amount of radiation to obtain a good signal-to-noise ratio even with a large electronic bandwidth, the apertures of the detection systems are relatively large. In some cases it is important to take into account these geometrical properties (beam widths of lines of sight). (d) A Be foil in front of the detectors is used to limit the photon energy range to with the system is sensitive. It has to be taken into account in the calibration and the interpretation of the measurements. Furthermore, because the filter characteristics depend on its thickness, and therefore on the angle of incidence, the dependence on the angle of incidence has to be taken into account in the geometrical properties.

The structure of this paper is as follows. The tomography method that we have developed is presented in Sec. 2. Various technical aspects, such as noise, uncertainties in the positioning, and the cross-camera calibration required because of neutron damage in the detectors is discussed in Sec. 3. Subsequently, the application of the tomography method to impurity injection (Sec. 4) and the study of ELM effects (Sec. 5) are presented. Section 6 discusses the results.

2. TOMOGRAPHY

Computerized tomography is a technique to reconstruct the local properties, e.g. emission or absorption, of an object from non-destructive external line-integrated measurements. The measurements of emitted radiation described in this paper are confined to one poloidal cross-section of the tokamak. In the prevailing electron and ion densities in the tokamak plasmas the plasma is optically thin for SXR radiation and refraction is negligible. Therefore, this paper is concerned with two-dimensional straight-line emission tomography without re-absorption.

2.1 Basic tomography methods

In two-dimensional tomography systems measurements are taken along lines of sight, and can essentially be represented by line integrals; i.e. the measurement f is given by straight-line integrals of the emissivity g as:

$$f(p,\xi) = \iint g(x,y)\,\delta(p + x\sin\xi - y\cos\xi)\,\mathrm{d}x\,\mathrm{d}y\,, \qquad (1)$$

where the integral is over the entire region where $g(x,y)$ is non-zero, and δ is the Dirac delta function. The line of sight is parametrized by p and ξ, p being the distance of the line to the

origin and ξ the angle of the line with the positive x axis. The tomography problem is the inversion of Eq. (1), which is an ill-posed problem [32,33]. Equation (1) is called the Radon transform. The parameters p and ξ are coordinates of a new space, which we will refer to as projection space. The measurements along straight *lines* can be considered to be values in *points* in projection space.

Equation (1) can be inverted analytically. Discretization of an analytical inversion formula gives rise to the so-called transform tomography methods [34], such as the Filtered Back-Projection (FBP) method which is widely applied in medical tomography. These methods are efficient, but are usually specific for a given regular coverage and are generally not very flexible. The other possibility is to discretize Eq. (1) before it is inverted. These methods are called series-expansion methods [23,35], one of which will be described in this paper. These methods are usually more flexible because additional information can easily be incorporated, the coverage does not need to be regular, and geometrical properties of the measuring system can be taken into account; but they are less efficient. Series-expansion methods are usually preferred over other methods in tomography on fusion devices due to the relatively small number of measurements (several hundreds), the irregular coverage due to restricted access, and the need for additional information to supplement the limited number of measurements. However, transform methods exist that overcome the problems associated with irregular coverage, see for example Ref. 36. The Cormack method mentioned in the introduction can be classified as either of the methods: an expansion is done into basis functions of which the inverse Radon transform is known. It differs from other series-expansion methods in that the processing ("a fit to the measurements") is done in projection space and not in actual space.

Equation (1) needs to be rewritten when imaging properties of the measuring system have to be taken into account. This can be done by including a geometric *function* $K_i(x,y)$ (note: one index) as a kernel in the Radon integral:

$$f_i = \iint g(x,y)\, K_i(x,y)\, \mathrm{d}x\, \mathrm{d}y\,. \tag{2}$$

Here, the quantities for each detector i are labelled with an index. In series-expansion methods Eq. (2) can be discretized by expanding g in basis functions b_j:

$$g(x,y) \approx \sum_j g_j b_j(x,y)\,. \tag{3}$$

This leads to the system of equations

$$f_i = \sum_j K_{ij} g_j\,, \tag{4}$$

where K_{ij} are the geometric *matrix* elements (note: two indices) which are obtained from

$$K_{ij} = \iint K_i(x,y) b_j(x,y)\, \mathrm{d}x\, \mathrm{d}y. \tag{5}$$

Note that in Eq. (3) the function $g(x,y)$ has been discretized into a one-dimensional vector $\boldsymbol{g}$. The usual basis functions are pixels. We, however, use basis functions that describe a bilinear interpolation between grid points, thus achieving a discretization that with Eq. (3) gives a continuous function $g(x,y)$ and hence is a more accurate discretization. The details of these basis functions are given in Appendix A.

2.2 The coverage of projection space, the geometric matrix, and the line-integral approximation

The coverage of projection space by the SXR tomography system is shown in Fig. 2(a). A uniform regular coverage of projection space is most adequate for tomography [32,37]. Due to the technical constraints in tokamaks this is usually not possible and the coverage of the current system is a good approximation, although there are some gaps. Due to the beam widths, each detector covers an area in projection space rather than a point. These areas are also indicated in Fig. 2(a), and are clearer in the blow-up in Fig. 2(b). The apertures of the cameras were chosen such that the region of the plasma which is viewed by each channel (the "beam width") reaches to the central line-of-sight of the neighbouring channels (camera V), or halfway to the neighbouring channels (other cameras).

In series-expansion methods the beam widths can be taken into account by means of the geometric matrix K_{ij} defined in Eq. (5). In a purely two-dimensional system, the geometric function $K_i(x,y)$ can be defined as the angle that the visible part of the detector spans as seen from the point (x,y). In three dimensions the equivalent can be defined by means of the *solid* angle. The quantity $K_i(x,y)/4\pi$ is then the fraction of the electro-magnetic radiation emitted in the point (x,y) that reaches detector *i*. However, in the application to *two*-dimensional tomography we have to assume that the emission is independent of the z direction perpendicular to the xy plane, which is usually possible in tokamaks because the toroidal extent of the viewing system is negligible compared to the sizes expected for toroidal structures in the emission. If, furthermore, the bending of the torus is negligible over the extent of the viewing system (i.e. the z axis is straight), we can define a function $k_i(p,\xi)$ as

$$k_i(p,\xi) = \iint \eta_i(p,\xi,z,\theta) \cos\theta\, \mathrm{d}\theta\, \mathrm{d}z, \tag{6}$$

where θ is an angle with respect to the xy plane and $\eta_i(p,\xi,z_1,\theta)$ the filter or transmission function of the detection system for a ray with direction (p,ξ) at angle θ through $z = z_1$. The

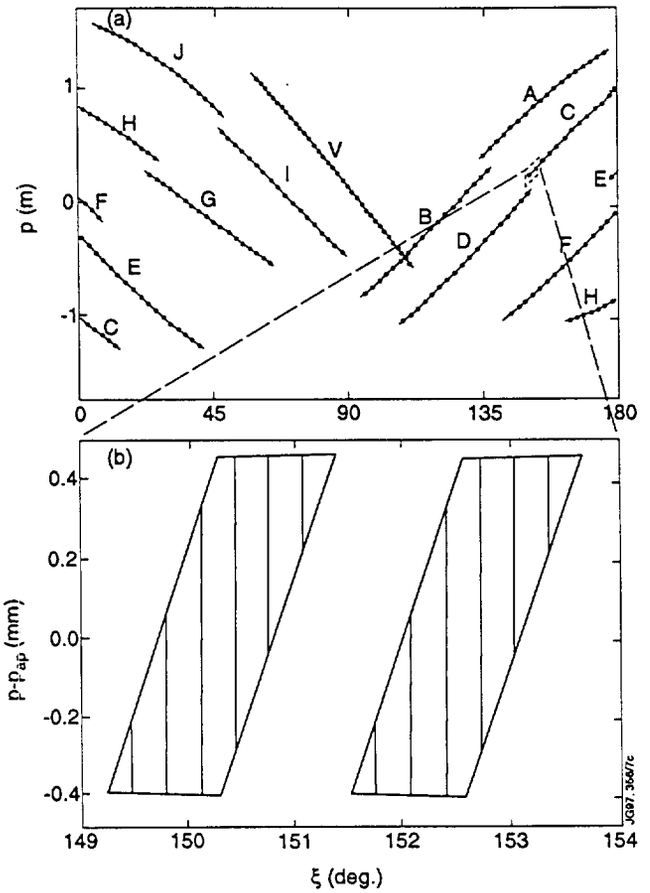

FIG. 2 (a) The coverage of projection space by the SXR tomography system. The solid circles indicate the average line-of-sight of each channel, and the area drawn around it (looking like lines) the total region covered due to the finite beam widths. (b) A blow-up of two regions covered by detectors [the area indicated by a dotted box in (a)]. To stretch the shape in the p direction, the p coordinate has been replaced by $p(\xi) - p_{ap}(\xi)$, where p_{ap} is the p of lines with varying ξ through the centre of the frontmost aperture. The contours indicate the contribution $k_i(p,\xi)$ from the third dimension, including the effect of the Be filter (contours in steps of 0.25% from the maximum, the maximum value being 10^{-3} rad m). The contours are vertical lines in this case because the aperture and the detector are parallel.

function η is zero for rays that are obstructed by an aperture or do otherwise not reach the detector. With this definition and the assumption of constant emissivity in the z direction, it can be shown that the geometric function can be written as [38]

$$K_i(x,y) = \int_0^{2\pi} \int_{-\infty}^{\infty} k_i(p,\xi)\, \delta(p + x\sin\xi - y\cos\xi)\, \mathrm{d}p\, \mathrm{d}\xi . \qquad (7)$$

To obtain the geometric matrix, an additional integral over x and y is required according to Eq. (5).

If η is unity, it is possible to calculate the geometric matrix directly as a full five-dimensional integral over the solid angle the detector spans (two integrals), and over x, y and z (each one integral), which is very time consuming. Calculation by means of Eqs. (5), (6) and (7) is

advantageous because of the following two points. Firstly, one can take advantage of the fact that the function $k_i(p,\xi)$ can be pre-calculated [i.e. it is constant on each line (p,ξ)], which reduces the number of dependent integrands significantly, see Ref. 38. Secondly, the filter function η of the Be filter can be taken into account fully, rather than having to use an average over the detector. Contour plots of the function $k_i(p,\xi)$ of two detectors are shown in Fig. 2(b). Because in the SXR system at JET the aperture and detectors are rectangular, the aperture-detector distance is relatively large compared to the detector size, and the filter function is not varying much over a detector, the function $k_i(p,\xi)$ is nearly constant for each detector. For a channel at the edge of the detector array the variation of the function $k_i(p,\xi)$ is only 1%, and even smaller for central channels.

When relevant emitting structures are present in the plasma that have sizes and characteristic lengths comparable to the regions covered by a single detector, it may be important to take the beam widths into account. This is only relevant for very peaked structures; most structures in the plasma are larger than these beam widths and the physical measurement f_i in Eq. (2) can therefore usually be approximated by line integral f of Eq. (1), multiplied by the étendue of the detector [38]. The étendue of the imaging system quantifies some of its properties: it is the solid angle from each point on the detector integrated over the detector surface. For the current system, the étendue calculated by a four-dimensional integral is close (within 1.5%) to an approximation of multiplying the detector surface by the solid angle that the aperture spans from the centre of the detector and applying a number of corrections for, for example, aperture thickness. A typical étendue of the system is $2\times10^{-8}\,\mathrm{m^2\,sr}$.

2.3 Constrained optimization

A large variety of methods exists to invert Eq. (4), some of which were mentioned in the introduction. The limited coverage of projection space restricts the types of tomography algorithms that can be applied. If a limited number of basis functions, often tailored to the physical problem, is sufficient to describe the problem and the system of equations is overdetermined, Singular Value Decomposition (SVD) can be used to find the least-squares solution. When the basis functions are pixel oriented the system of equations is usually underdetermined. In the past the Algebraic Reconstruction Technique (ART) [23] and many variations have been applied, which are iterative techniques. This has not been successful on tomography of fusion plasmas, except when thousands of measurements were available [39]. The problem is that the measurements themselves do not describe a unique solution and the solution is sensitive to noise (i.e. the problem is ill posed). Regularization is required by taking into account additional information to obtain a single well-behaved solution. This can be done between the iterations in ART, or by limiting the number of basis functions to make the system overdetermined. However,

regularization can be applied in a mathematically more correct way in so-called constrained optimization methods. When the number of pixels is not larger than several thousands, as is the case in our problem, it is feasible to solve the system of equations non-iteratively.

For the constrained optimization we define an object function $O(\boldsymbol{g})$ that describes a quality of the emission profile $\boldsymbol{g}$ that we expect to be small for physically feasible profiles. For example, the smoothness of the emission profile or low emissivity outside the plasma region may be included in the object function. Defining an estimated error vector ε, we expect the misfit between the measurements $\boldsymbol{f}$ and backcalculated measurements $K\boldsymbol{g}$ to be

$$\left\|\boldsymbol{f} - K\boldsymbol{g}\right\|^2 \leq \|\varepsilon\|^2 .$$

The tomography problem can then be stated as follows: we minimize the object function under the constraint $C(\boldsymbol{g})$:

$$C(\boldsymbol{g}) = \left\|\boldsymbol{f} - K\boldsymbol{g}\right\|^2 - \|\varepsilon\|^2 \leq 0 . \tag{8}$$

The constrained optimization can be solved by the Lagrange multiplier method, i.e. the following conditions have to be satisfied:

$$\begin{aligned} &\frac{\partial}{\partial \boldsymbol{g}} O(\boldsymbol{g}) + \lambda \frac{\partial}{\partial \boldsymbol{g}} C(\boldsymbol{g}) = 0, \\ &\lambda C(\boldsymbol{g}) = 0, \\ &\lambda \geq 0, \\ &C(\boldsymbol{g}) \leq 0. \end{aligned} \tag{9}$$

Here, λ is the Lagrange multiplier. In the following, Dirac notation will be used for scalar products and the like. If the object function is quadratic, in particular $O(\boldsymbol{g}) = \langle \boldsymbol{g} | \Omega | \boldsymbol{g} \rangle$ where Ω is a matrix, Eq. (9) results in a matrix equation

$$\left(\lambda K^{\mathsf{T}} W K + \Omega\right)\boldsymbol{g} = \lambda K^{\mathsf{T}} W \boldsymbol{f} . \tag{10}$$

Here, K^{T} is the transpose of K. Furthermore, a weighting matrix W has been introduced that is the inverse of the covariance matrix. When noise in the measurements can be assumed to be uncorrelated, a point we will return to later, W is given by

$$W_{ii} = 1/\varepsilon_i^2 \text{ and } W_{i \neq j} = 0 .$$

Equation (10) is solved with the constraint $C(g) \leq 0$. With the weighting matrix W, Eq. (8) should be modified to $C(g) = \langle f - Kg | W | f - Kg \rangle - \langle \varepsilon | W | \varepsilon \rangle$, where $\langle \varepsilon | W | \varepsilon \rangle = I$: the number of detectors.

This approach with the Lagrange multiplier method is equivalent to the regularization approach from the theory of ill-posed problems, described in, for instance, Refs. 27,30,33 and 40. These methods minimize

$$\|f - Kg\|^2 + \alpha O(g),$$

where the regularization parameter α is equivalent to $1/\lambda$. Various approaches to find a good regularization parameter have been suggested (which depend, for example, on the number of available channels, on the noise level, and on statistical properties of the measurements) [33,41,42]. In our opinion the constraint given by Eq. (8) is physically meaningful: we cannot trust the measurements within the measurement error, and if no fit to the measurements can be found within these errors, something must be wrong with the measurements or the estimate of the error. It has been argued that, given measurement errors ε, the constraint $C(g) \leq 0$ is too pessimistic [26,33]. We will come back to this matter when discussing uncertainties in the measurements.

It is possible to add additional constraints to the optimization problem, for example

$$g_j \geq 0 \quad \text{for all } j, \tag{11}$$

i.e. non-negativity. It is also possible to use minimum values other than zero, or maximum values, if information about the level of emission in certain parts of the plasma is known in detail from other diagnostics. Additional Lagrange multipliers l_j (written as a vector $\boldsymbol{l}$) are introduced.

2.4 Method of solution

Equation (10) and the Lagrange multipliers should be solved, given the constraints. The following shorthand notation will be used: $C = K^T W K$, $c^T = -K^T W f$, $B = \Omega$, and Dirac notation for scalar products. Equation (10), including the non-negativity constraints, can now be written as

$$(B + \lambda C)g = \boldsymbol{l} - \lambda c. \tag{12}$$

It is possible to solve Eq. (12) formally by considering a generalized eigenvalue problem [43], see Appendix B. If the matrix B (i.e. Ω) is positive definite, the analytical solution of Eq. (12) can be expressed in terms of the generalized eigenvectors $|y_k\rangle$ and eigenvalues μ_k, k=1...J where J is the number of grid points, as [43]

$$|g(\lambda)\rangle = \sum_{k=1}^{J} \frac{\langle y_k|l\rangle - \lambda\langle y_k|c\rangle}{1+\lambda\mu_k}|y_k\rangle. \tag{13}$$

This is the solution without imposed constraints, i.e. a function of λ. Given the l, the λ that solves the of the *constrained* optimization problem is the root of [43]

$$C(g(\lambda)) = \langle f|W|f\rangle - \langle \varepsilon|W|\varepsilon\rangle - \sum_{k=1}^{J} \frac{(\mu_k\lambda^2 + 2\lambda)\langle c|y_k\rangle^2 - \mu_k\langle l|y_k\rangle^2 - 2\langle l|y_k\rangle\langle c|y_k\rangle}{(1+\lambda\mu_k)^2} = 0. \tag{14}$$

It can be shown that, for $\lambda > 0$, C is a monotonically decreasing function with λ [43], i.e. there is a unique solution, which means that Eq. (14) can be solved numerically in a straightforward way.

The non-negativity constraints of Eq. (11) can be implemented in an iterative way [43]. First we solve the problem with $l = 0$. Only the constraints where this initial solution violates the constraints need to be considered, i.e. we only use the Lagrange multipliers l_j corresponding to negative grid points. We modify these Lagrange multipliers in such a way that the solution of Eq. (13) satisfies the constraints. This involves solving a system of equations of which the dimensions are those of the number of violated constraints; consequently this is fast if there is only a small number of violated of constraints. These new l_j are used to find a new root λ of Eq. (14), which possibly results in a solution g that violates some other constraints. This process is iterated until a solution is found that satisfies all constraints. Although convergence cannot be guaranteed, especially when an attempt is made to reconstruct inconsistent data for which no positive solution might exist, the method generally works well. This method is not iterative in solution space, but is an iterative search for active constraints in the space of Lagrange multipliers, which can be much faster.

An alternative method to solve the constrained optimization method is to solve Eq. (10) iteratively in solution space for given λ, modifying λ until the solution agrees with the constraints. Despite a matrix inversion in each iteration (generally fewer than 10 iterations are needed to obtain convergence), this method is in practice about a factor of two faster than the generalized eigenfunction method, which involves only one time-consuming solution. However, the non-negativity constraint is only available in the latter. Furthermore, having an analytical expression for the inverse as a function of λ [Eq. (13)] means that, as long the geometry and smoothness matrices remain the same, the solution can quickly be found for many sets of measurements, in seconds rather than the minutes required for each case with the iterative method on an IBM RS6000 workstation for a grid with about 1200 points.

2.5 Choice of object function

The object function to regularize the solution of the ill-posed problem should incorporate *a priori* information obtained from physical considerations of the expected solution. Usually we will expect the emission to be a smooth function in the poloidal cross-section and the emission to be zero outside the separatrix. The implementation of anisotropic smoothness, smallness at the edge, and a way to prevent oversmoothing of peaks are discussed

Common regularizations in the literature are: (a) Phillips-Tikhonov regularization in which the norm $\|\boldsymbol{g}\|$ or some other scalar quality such as overall smoothness is minimized (see Appendix C), and (b) maximum entropy where $O(\boldsymbol{g}) = -\sum_j g_j \ln g_j$ is maximized [26,44] (note: this object function is nonquadratric and can therefore not be solved by the matrix approach described here). We will only consider an object function related to smoothness because we obtain adequate results with it. In plain language, the optimization by means of the smoothness object function can be stated as follows: find the smoothest function for which the misfit is equal to the estimated noise.

Although smoothness as it is usually implemented in the literature (see Appendix C) gives reasonable results, a better fit to the measurements and more likely reconstructions from the physical point of view are obtained with the following object function. We know that the SXR emission in a tokamak, to the first order, is a flux function; for example, the discrepancy in the elongation is smaller than 10% [45]. Therefore, we expect the emission profile to be smoother in the poloidal direction than in the radial direction. This idea can be stated as an anisotropic diffusion equation, which was introduced successfully to bolometer tomography [30]. The object function describing the overall diffusion in the reconstruction region is

$$O(\boldsymbol{g}) = \langle \boldsymbol{g} | \Omega | \boldsymbol{g} \rangle = \iint \left\{ \nabla \cdot \left[\mathbf{D}_{\mathrm{D}} \cdot \nabla g(x,y) \right] \right\}^2 \mathrm{d}x\,\mathrm{d}y =$$

$$\iint \left[\nabla \cdot \left(\boldsymbol{n} D_{\perp} \boldsymbol{n} \cdot \nabla g + \boldsymbol{t} D_{//} \boldsymbol{t} \cdot \nabla g \right) \right]^2 \mathrm{d}x\,\mathrm{d}y\,, \qquad (15)$$

where $\mathbf{D}_{\mathrm{D}}$ is an anisotropic diffusion tensor which is given by the parallel and perpendicular diffusion coefficients $D_{\perp}$ and $D_{//}$. The vectors $\boldsymbol{n}$ and $\boldsymbol{t}$ are the unit vectors normal and tangential to the flux surfaces in the poloidal cross-section. Note that this diffusion tensor is a purely mathematical quantity used to introduce anisotropic smoothness, which is only remotely related to transport diffusion coefficients in the plasma. Instead of indicating the *smoothest* solution, the functional of Eq. (15) is small for the solution that would give the *least diffusion*. Choosing Cartesian coordinates, Eq. (15) can be expressed in terms of derivative matrices D (see Appendix C) in matrix form to give

$$\Omega = \left(C_x D_x + C_y D_y + C_{xx} D_{xx} + 2C_{xy} D_{xy} + C_{yy} D_{yy}\right)^{\mathrm{T}} F \times \left(C_x D_x + C_y D_y + C_{xx} D_{xx} + 2C_{xy} D_{xy} + C_{yy} D_{yy}\right) \times \Delta x \Delta y + C_0, \tag{16}$$

where the C are diagonal matrices of which the diagonal elements are complicated, but well-defined, functions of the diffusion coefficients, the flux function, and their derivatives. The additional diagonal matrices F and C_0, which do not follow from Eq. (15), will be discussed later. The distances between grid points in the x and y directions are given by Δx and Δy.

It should be stressed that the anisotropic diffusion object function is not a strict prescription of the solution. The object function becomes larger the more it deviates from an emission profile with minimum diffusion. If the anisotropic diffusion assumption is not supported by the measurements, still a solution which fits the data will be found. If one would use flux coordinates, the solution would be more restricted than by only the object function. Errors could occur when, for example, the magnetic equilibrium solution is not sufficiently good or when the emission is not a flux function. One reason for using Cartesian coordinates is, therefore, that these are more flexible. Another reason is that the implementation of derivative matrices is far simpler. Some details are discussed in Appendix C.

It is possible to add a requirement of smallness of emission in certain grid points to the object function by the diagonal matrix C_0 in Eq. (16) (see also Appendix C). This has been done for grid points in the boundary of the reconstruction region (points far outside the plasma). The coefficients have to be chosen in relation to the other part of the object function to give realistic results. A further advantage of the C_0 term is that it makes the matrix Ω of full rank, thus positive definite. This makes it possible to use more efficient solution algorithms than for a positive-semidefinite matrix, and it may make the solution more well behaved by removing small positive and negative eigenvalues that can result from numerical errors.

We have found that due to the relatively large estimated errors, which are consistent with the uncertainties in the measurements, too smooth reconstructions are obtained for very peaked emission profiles, i.e. the peak values are too low. This can be prevented by assuming smaller estimated errors for the channels that see the peak emissivity, because the measurements are weighted by their error by means of the matrix W. However, this is not a satisfactory solution, because errors in the peak measurements will produce artefacts. Another way of preventing the oversmoothing of peaks is by introducing a diagonal matrix F in Eq. (16), that reduces the contribution of peaks to the object function. In Ref. 27 this method has been described as a linearization of the minimum Fisher information quantifier, when used with first derivative matrices. There, $F_{jj} = 1/\, g'_j$ was used, where g'_j is the solution of a previous reconstruction, so that the object function remains linear. We found that this did not give satisfactory results in combination with the minimum diffusion: the peaks were not followed well, and the behaviour

of small and slightly negative values was unpredictable. An implementation that worked satisfactorily was

$$F_{jj} = \begin{cases} (\overline{g'} / g'_j)^{\beta} & \text{for } g'_j \geq \gamma\overline{g'}, \\ 1 & \text{for } g'_j < \gamma\overline{g'}, \end{cases}$$

where $\overline{g'}$ denotes the average reconstructed emissivity and β and γ are parameters. We use typically β=2...3 and γ=1...1.5. After one or two iterations, replacing g'_j by the most recent reconstruction, hardly any change is observed in the solution, which means that convergence is very rapid.

2.6 Practical implementation

The matrices involved in the constrained optimization method are huge. The dimension of the matrices $K^{\mathrm{T}}WK$ and Ω is $J \times J$, where J is the number of grid points. With J of the order of 1000, several tens of Mbyte of computer memory is required. However, the matrices are very sparse with typically only a few percent nonzero elements. We have implemented a sparse storage method in which matrix multiplications such as $K^{\mathrm{T}}WK$ can be carried out efficiently, i.e. only considering multiplications with nonzero elements. This not only saves memory space, but also speeds up the pre-processing of the matrices by several orders of magnitude compared to standard matrix multiplication. The solution of Eq. (10) or the generalized eigenvalue problem described in Appendix B is done by routines of the NAG package [46], for which the matrices have to be expanded to normal storage. Although the matrices are very sparse, due to the asymmetrical coverage of lines of sight and the inclusion of the magnetic flux function in the calculation of Ω, the matrices do not have a clear structure that one could take advantage of by means of specialized solution techniques for sparse matrices.

The grid size is based on the number of measurements, on the available memory, and on the maximum acceptable reconstruction time. Originally a rectangular regular grid was used. This was not sufficiently flexible and had a large number of grid points outside the plasma where no emission is expected. Therefore, a method was developed to make varying grid sizes possible, depending on the average distance between lines of sight in a region and the required spatial resolution, without increasing the memory usage. Particular care had to be taken in the calculation of the derivative matrices and the basis functions on the boundaries between regions with varying grid size.

Apart from the C_0 term in the object function to ensure a low emission outside the plasma, it has also proved advantageous to add a number of virtual lines of sight outside the plasma which "measure" zero values. Although it is possible to vary the ratio $D_{\perp}/D_{//}$ for various parts of the reconstruction region, this is not done for most SXR reconstructions. The ratio $D_{\perp}/D_{//}$ is

typically chosen as 0.1. The effects of all these parameters on reconstructions have been tested by means of phantom calculations. Important other parameters are the estimated errors and the cross-camera calibration factors, which are discussed next.

3. TECHNICAL ASPECTS AND PROCESSING OF MEASUREMENTS

To be able to interpret the measurements correctly and to carry out tomographic reconstructions, some properties of the measurement system have to be considered. The correction for beam-width effects were discussed in Sec. 2.2. Other aspects are the Be filters and calibration, and uncertainties in the positioning of the detectors. Furthermore, it is important to determine which estimated errors to use in the reconstruction and to correct for the varying sensitivities due to neutron damage on the detectors.

3.1 Be filters and calibration

The detectors, which may also be used as sensors in the visible range, are sensitive to a large part of the electromagnetic spectrum. A filter is used to select the SXR range. This is done by placing a Be foil in front of the detector. In JET a flat foil with a thickness of 250 μm is used, which results in high-pass filtering at 2 keV. The detector itself is sensitive to this radiation, but its sensitivity starts to fall off above about 8 keV. This fall-off is not known exactly due to discrepancies in models that predict the sensitivity and due to a lack of suitable calibration sources. Because the measurement is integrating over the range 2 to about 10 keV, it is not possible to spectrally resolve the measurement. To obtain an absolute calibration, it is therefore necessary to assume the spectrum emitted by the plasma. The assumption is that the plasma radiates bremsstrahlung at a temperature of 10 keV. The calibration factors obtained hardly depend on the high-energy cut-off by the detector sensitivity, and depend only mildly on the change of the spectrum as a function of the electron temperature of the plasma. Except at the edge of the plasma, where SXR emission is low anyway, the calibration factors are therefore adequate to calculate the absolute emission level. However, in particular cases, for example when the emission does not follow the bremsstrahlung continuum spectrum, it may be required to take into account the filter function more properly in the interpretation of the measurements. Angular geometrical effects due to the Be foils being flat were discussed in Sec. 2.2. In this treatment of angular effects only the decrease in absolute filter value is used, i.e. integrated over the spectrum.

3.2 Positioning

For tomography it is very important to know the positions and lines of sight of the detectors accurately. The directions of the lines of sight and the detector-aperture distance were measured by means of a laser to within some millimetres with respect to a reference point on the flange

that is attached to the camera housing. After mounting the cameras on the tokamak, the positions and angles of the flanges were measured with respect to a common reference point. Although the measurements were done at room temperature and the vessel is operated at an elevated temperature, the change of the angles is negligible and the shift of about 3 mm due to heat expansion is similar for all cameras. Overall, the uncertainty in relative positions of lines of sight of different cameras is 1–2 cm at the plasma centre. Comparison of measurements by different cameras of localized emission, e.g. very peaked emission in the centre or peaks in emission from the wall (Sec. 5), shows that the measurements are consistent with this uncertainty. Compared to the machine size these uncertainties are very small (the minor radius is of the order of one metre) and they are also much smaller than the grid size used in the tomographic reconstructions (7.5 cm).

3.3 Estimated errors

The estimated errors must describe the uncertainties in the measurements. These include noise and pick-up from the electronics and the measurement system, the contribution from emitting structures in the plasma that are smaller than can be resolved by the system, uncertainties in the positioning, uncertainties in the calibration, and discretization errors.

The noise-equivalent power (NEP) level is typically 2–8 W/m^2, to be compared to signal levels of 20 W/m^2 for channels viewing the edge of the plasma, and more than 1 kW/m^2 for central channels. For all but the channels most to the edge the noise is due to photon statistics [11]. However, especially during phases with MHD activity, plasma fluctuations of structures smaller than can be resolved by tomography, which can give a contribution of a few percent of the signal, will have to be considered as noise from the tomography point of view. Uncertainties in the positioning can lead to uncertainties as large as 10% for steep emission profiles. Geometrical calibration factors are probably accurate within 2%. The sensitivity of detectors is assumed to be constant over detector arrays. Uncertainties in the cross-camera calibration are discussed in the next subsection. These numbers give rise to an overall uncertainty of 3% to 4% in the measurements, including the uncertainties in cross-camera calibration. When this uncertainty is applied as estimated error in the tomographic reconstruction under varying plasma conditions relatively smooth profiles are obtained without artefacts. If the estimated errors are chosen to be smaller, small structures appear in plasmas that are expected to have smooth emission profiles. When significant structures that change during the plasma discharge are found in the tomographic reconstructions, using estimated errors of 3% to 4%, these structures are believed to be real. Admittedly, one cannot be absolutely certain about such structures from tomographic reconstructions alone, and appropriate error bars have to be taken into account in the interpretation.

In the weighting by a diagonal matrix W in Eq. (10) it is assumed that the noise of channels is uncorrelated. This is only true for noise arising from the electronics and the detection system. Although it is possible to use the full covariance matrix for W rather than only the diagonal [47],

we expect its inclusion only to give very minor changes, given the other uncertainties discussed above. Furthermore, the reasonable estimated noise level has been found by comparing many tomographic reconstructions. Therefore, the argument that the constraint Eq. (8) is too pessimistic is therefore not relevant in our case.

3.4 Neutron damage correction

In JET high-performance deuterium plasmas high neutron fluxes are generated. Although this does not amount to a significant background signal, the fluences of neutrons, which are typically 10^{15} neutrons/m^2 for each high-performance pulse and about 4×10^{17} neutrons/m^2 for the entire time the detectors have been operational [11], result in an appreciable radiation damage to the detectors. Detectors close to the plasma suffer most damage. This damage changes the sensitivity of the detectors. Because it is not possible to re-calibrate the detectors in the SXR range inside the vessel, the cross-camera calibration had to be achieved by comparing measurements from the various arrays.

If full projections are available, i.e. a view from one direction that covers the entire plasma cross-section, the total radiation can be estimated, and normalizing all views to the same total radiation achieves a cross-calibration. Unfortunately, due to mechanical constraints, the JET SXR system views the plasma in fans that do not all see the entire plasma. Furthermore, most of the views consist of two cameras. If the neutron damage can be assumed to be the same for the two cameras of a view and the SXR emission is approximately constant on flux surfaces, it is possible to make separate Abel inverses of each view, and derive the correction factors by comparing the obtained radial profiles. This method gives a starting point for further fine-tuning of the correction factors. It was found that different correction factors were needed for each individual detector array.

The way followed to find the optimum correction factors was the following. A tomographic reconstruction was made with a certain combination of correction factors applied to the measurements, and the quality of the reconstruction was assessed. Because the SXR system has a sufficiently good coverage of the plasma to be able to make reconstructions of most emission profiles without negative values (without using the non-negativity constraint), the amplitude of negative artefacts in the reconstruction is a good quantifier of the quality of the reconstruction. Also the achieved fit of backcalculated measurements to the corrected measurements indicates for which cameras unrealistic correction factors are used [for which the matrix F of Eq. (16) proved useful]. Further, more subjective, quality criteria are the absence of large unexpected structures and structures outside the plasma. It was possible to minimize these artefacts by changing correction factors by hand, but also to further optimize the solution by randomly varying the correction factors (in a Gaussian band around the first estimate) in hundreds of reconstructions and then picking the best. Figure 3 shows a typical example of the effect of the correction factors and the quality of the tomographic reconstruction (i.e. the close fit between measurements and

backcalculated measurements). The main justification for this procedure is that the correction factors found in one time slice also give good results for other time slices in the same discharge even when the emission profile changes drastically, which gives us confidence that the reconstructions obtained are good representations of the actual emissivity.

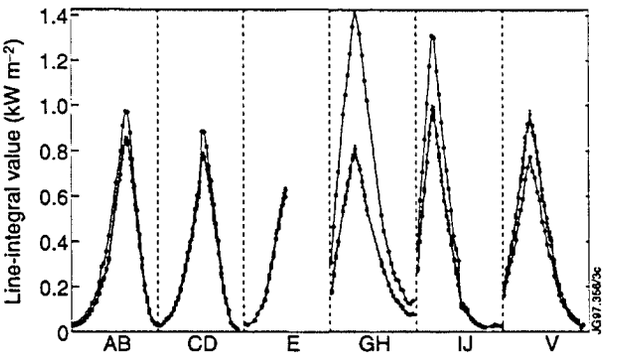

FIG. 3 Typical example of the raw measurements of all channels in one time slice (open circles), the values corrected for neutron damage (solid circles; the error bars indicate the estimated errors), and the backcalculated values from the tomographic reconstruction (solid squares connected by dashed lines). The numbering of detectors per combination of two cameras is clockwise. Camera F was not available in this discharge. This particular example is the time slice at the time of Ni injection of the case in Fig 5.

Because of the required magnitude of correction factors, the tomographic reconstructions have an uncertainty of about a factor two in absolute values. Apparently, effects such as a varying heat load during a discharge have little effect on the sensitivity. However, for different discharges the correction factors werefound to vary. In the 1994-1995 campaign a gradual decrease in sensitivity of the detectors was observed, the sensitivity of detectors close to the plasma decreasing most [11]. For the 1996-1997 campaign batteries were installed to apply a reverse bias over the detectors, which should reduce the fall in sensitivity [11]. Because at elevated temperatures the damage is reduced by annealing and several other effects, it is difficult to predict the change of sensitivity. In the 1996-1997 campaign there is not a clear trend in changes in the correction factors over a long time span, although the differences between cameras get larger over time. In most recent discharges there are apparent artefacts that do not disappear when the correction factors, which are taken as constant over the detector arrays, are varied. This is probably due to a variation of damage over the arrays. We have not attempted to correct for this variation in sensitivity, because the determination of the required number of free parameters with the above method can hardly be justified. The remaining artefacts have much smaller values (<10%) than the features presented in this paper. However, the amplitudes have levels comparable to, for example, MHD oscillations, which makes this particular tomography algorithm unsuitable for studying such phenomena. During DT operation, in which the neutron fluences increased by a factor of 50 and the average neutron energy by a factor of 6, the detectors were expected to be damaged to such an extent that no subsequent useful measurements would be possible. Although the damage has increased dark currents significantly (a dependence of the dark currents on the toroidal magnetic field is observed), surprisingly, it is still possible to obtain reasonable tomographic reconstructions after corrections for the dark current and the degraded sensitivity.

4. SXR EMISSION AFTER NI INJECTION

In JET, particle transport can be studied by injecting non-recycling metallic trace impurities into the plasma by means of laser blow-off. Nickel is a much used impurity for this purpose, since even small quantities that do not appreciably change the plasma parameters, give a significant increase in SXR emission, in some cases doubling the emissivity. Typically, the Ni concentration is 0.01–0.05% of the electron density, which justifies the assumption that the Ni atoms behave as test particles without collective behaviour. The emission seen by the SXR tomography system is mainly (>85%) due to the recombination radiation and the K_α line of the Ni^{26+} ionization stage. The emission after subtraction of the SXR radiation level of before the injection is therefore approximately proportional to the Ni^{26+} density. The emission can be simulated and matched by transport codes. This is a very powerful method because the simulations can be compared directly with the *local* emissivity, rather than having to rely solely on comparison with smeared out line-integrated spectroscopic measurements, as has been the case in earlier transport studies. Therefore, SXR tomography plays a key role in the evaluation of the experiments. Since the 215-channel SXR system has been operational on JET, dedicated Ni-injection experiments have been carried out in two high-performance plasma regimes: hot-ion H modes and so-called optimised-shear discharges. The cases studied are not in steady state, complicating the interpretation. Together with improvements in the analysis method [48], the current JET SXR system and processing make it possible to achieve unprecedented resolution, detail and accuracy.

4.1 Tomographic reconstructions

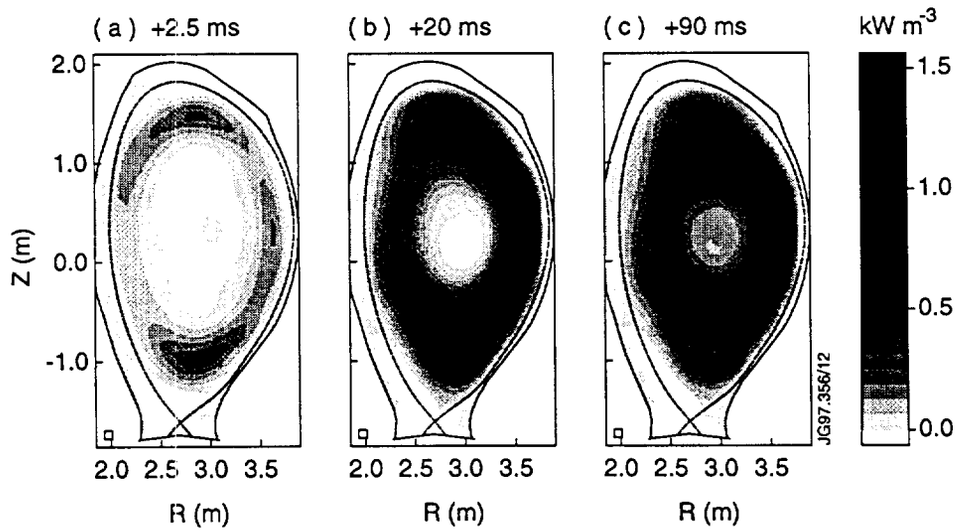

FIG. 4 Background subtracted SXR emission in a poloidal cross-section from tomographic reconstructions at three time slices after Ni injection (t=0ms) into an ELM-free hot-ion H mode (JET discharge 34476). The R *coordinate is the major radius and* Z *is the vertical coordinate. The square in the lower-left corner indicates the grid size and the dashed line the separatrix.*

Figure 4 shows SXR images during Ni injection into an ELM-free H mode plasma. A slope fitted to the times before the injection is taken as an estimate of the evolution in time of the

background SXR emission and has been subtracted to give purely the contribution of Ni to the SXR emission. Although it is an ELM-free H mode, an ELM at the time of the injection [49] causes rapid Ni transport compared with cases without ELMs. The reconstructions did not require the non-negativity constraint, but the full geometric matrix helped to make the profiles somewhat more peaked. Two important features can be observed in Fig. 4. The most salient feature is the in-out asymmetric crescent-shaped emission peak. This has been reported several times in the literature [50–53]. This asymmetry is well understood as being caused by the centrifugal force due to fast toroidal rotation of the plasma (faster than the thermal velocity of Ni ions), which has a profound impact especially on heavy impurities. The reconstructions and theoretical predictions agree very well quantitatively [52,53]. The other characteristic signature of this Ni injection is the rapid inward movement (~10 ms) of the radiating ring, which thereafter remains stationary at mid radius for a long time (>100 ms).

In discharges in the so-called optimized-shear regime [54], which have very peaked electron density and temperature profiles, the emission profile behaves very differently (Fig. 5). In this type of discharge the peak of the SXR emission moves quickly inwards, reaches the centre in about 70 ms and decays afterwards.

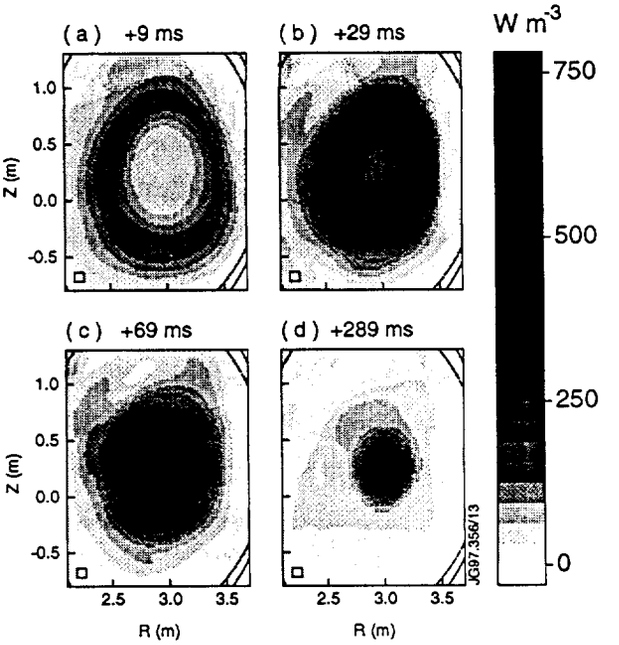

FIG. 5 Background subtracted SXR emission in a poloidal cross-section from tomographic reconstructions at four time slices after the Ni injection (t=0 ms) into an optimized-shear discharge (JET discharge 38441). The same conventions as in Fig. 4 have been used.

4.2 Transport simulations

The time scales of movement of the radiating ring give insight into transport of impurities in the plasma. This is studied in detail by means of one-dimensional transport codes. Therefore, the tomographic reconstruction has to be transformed into a radial profile. This is done by means of the background-subtracted flux-surface averaged] emissivity $\Delta\varepsilon$ as a function of the normalized minor radius ρ. The flux surface averages of Figs. 4 and 5 are shown in Figs. 6(a) and 7(a). Because the tomographic reconstructions cannot be verified directly with other diagnostics, the error bars for two of the time slices have been determined by varying reconstruction parameters within reasonable limits, such as the estimated errors (1.5–4%), the correction factors, the grid size, and the ratio $D_\perp / D_{//}$ (between 0.01 and 1). Furthermore, the effects of using the smoothness discussed in Appendix C instead of Eq. (16), including the matrix F of Eq. (16), using a

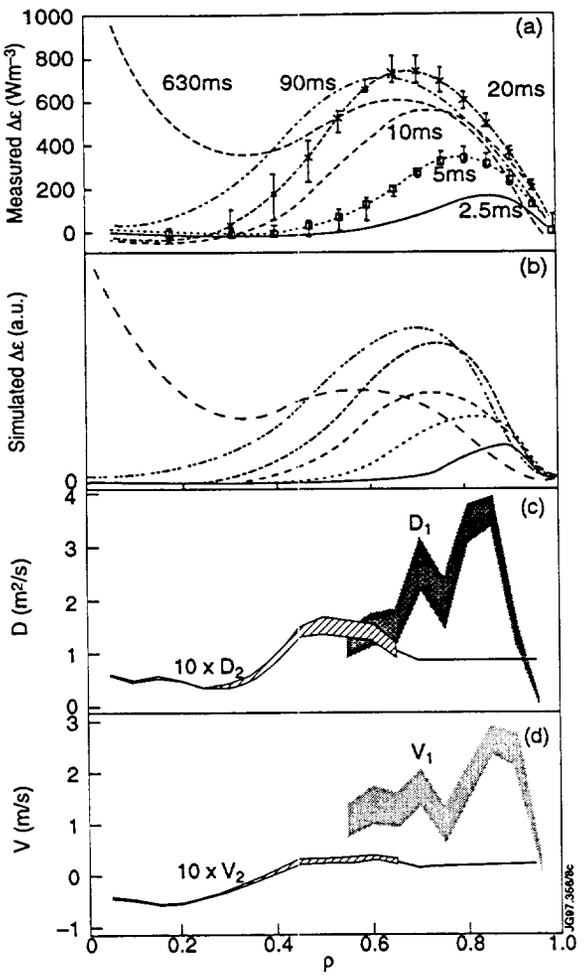

FIG. 6 (a) Background subtracted flux-surface averages Δε of tomographic reconstructions of the hot-ion H mode of Fig. 4 as a function of minor radius. (b) Simulated Δε for the same times. (c) Diffusion D *and (d) convection velocity* V *as a function of the normalized minor radius found from the simulation.* D_1 *and* V_1 *are during the first phase following the ELM;* D_2 *and* V_2 *are for the subsequent quiescent phase.*

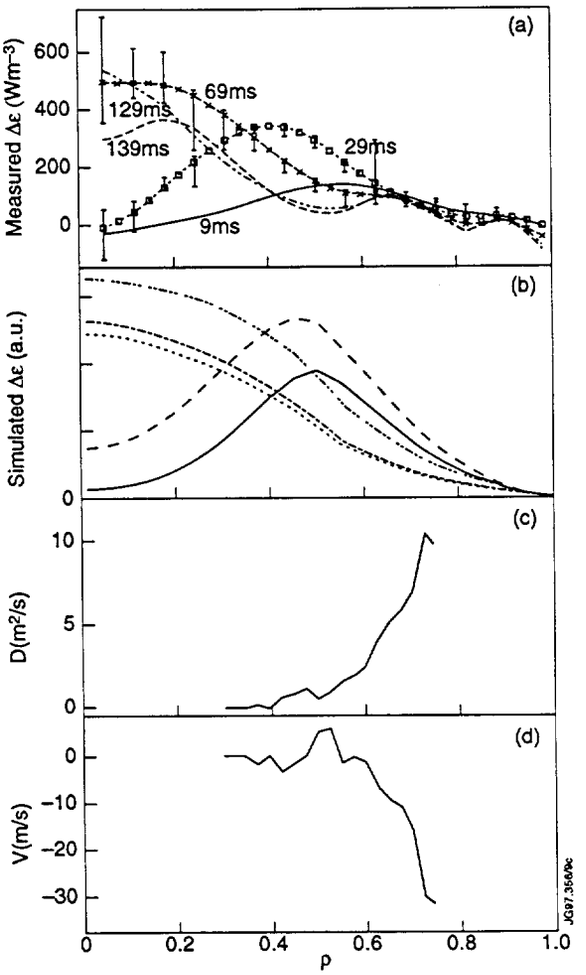

FIG. 7 (a) Background subtracted flux-surface averages Δε of tomographic reconstructions of the optimized-shear discharge of Fig. 5 as a function of minor radius. (b) Simulated Δε for the same times. (c) Diffusion D *and (d) convection velocity* V *as a function of the normalized minor radius found from the simulation in the first phase after the injection.*

pure line-integral geometric matrix, and applying the non-negativity constraint were studied and are taken into account in the error bars. Clearly, the observed effects are much larger than the error bars.

The flux-surface averaged perpendicular flux Γ_z of the trace impurity, with density n_z, is assumed to be of the form

$$\Gamma_z(\rho) = -D(\rho)\frac{\partial n_z}{\partial \rho} + V(\rho) n_z(\rho), \tag{17}$$

where ρ is the minor radius, and D and V are the diffusion coefficient and convection velocity, respectively. Here, D is the so-called circular-equivalent diffusion coefficient, which is related to

the diffusion coefficient D_C in Cartesian coordinates by $D = \langle |\nabla \rho|^2 \rangle D_C$, where the brackets denote the flux-surface average. The electron density n_e and temperature T_e are assumed to be constant on flux surfaces. The incremental SXR emission due to the injected impurity can be written as

$$\Delta\varepsilon = \sum_l n_e n_{Zl} Q_{Zl}(T_e, f_l) = n_e \langle n_Z \rangle Q_Z, \tag{18}$$

where l indicates the charge state, f_l the fractional abundance of the stage, and Q_Z is a coefficient that takes into account all relevant atomic processes, calculated from a collisional-radiative model including the specific filter of the SXR system. The radial profiles for D and V are obtained from a fit to Eq. (17), where n_z has been calculated from Eq. (18) with an initial guess of Q_Z and the experimentally determined $\Delta\varepsilon$. This process is iterated, using the found D and V to calculate a new Q_Z, until convergence is reached and a good fit is obtained to the temporal evolution of several spectral lines of Ni measured by spectrometers. This iterative procedure is described extensively in Ref. 48. The validity of the ansatz Eq. (17) is demonstrated by the straight lines that can be fitted for various radii, as shown in Fig. 8. The incremental emissivity $\Delta\varepsilon$ obtained from the simulations for both the cases is given in Figs. 6(b) and 7(b). The transport parameters found are shown in Figs. 6(c–d) and 7(c–d). The error bars (shaded regions) are obtained from a statistical analysis of the fit to Eq. (17), including the error bars in $\Delta\varepsilon$. Uncertainties in n_e and T_e will have an influence as well, but will not significantly alter the results. At the edge $\Delta\varepsilon$ is so small due to the low SXR emissivity that D and V cannot be determined accurately [48].

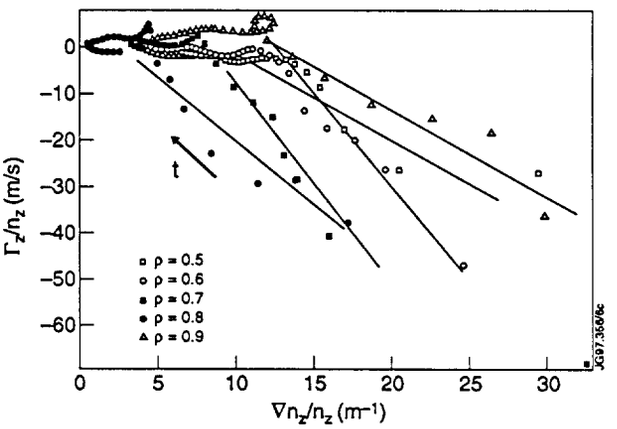

FIG. 8 Normalized fluxes Γ_z / n_z against the normalized density gradient ∇n_z / n_z for five radial positions. Time can be thought to increase along the lines in the upward direction. The fitted slope gives the D(ρ) *and the crossing on the flux axis the* V(ρ).

4.3 Results

In the hot-ion H mode (Fig. 6) two very distinctive phases can be distinguished. In the first phase, 10–12 ms following the ELM, the diffusivity is very high ($D \approx 4\,\mathrm{m^2/s}$ around $\rho = 0.7 - 0.8$) and the convection velocity appears to be directed outward. In cases where no ELM occurs at the time of injection, the transport in the outer layers in considerably smaller. This is followed by a second phase, when the Ni has reached $\rho \approx 0.7$, in which the transport has slowed down: the diffusivity is small ($D < 0.2\,\mathrm{m^2/s}$) in the entire plasma and very small ($D \approx 0.05\,\mathrm{m^2/s}$) in the

inner core, where it is close to neoclassical predicted values. The Ni is driven by convective effects and may reach the centre after hundreds of milliseconds.

In optimized-shear discharges (Fig. 7), an internal transport barrier (ITB) is formed at $\rho = 0.5 - 0.7$ (contrary to the H modes where there is a transport barrier at the very edge), which, inside the barrier, leads to a very peaked electron and ion temperature profiles, usually also a very peaked electron density profile, a low ion thermal diffusivity and high fusion yields [54]. This discharge is not in steady-state: the ion temperature was still growing at the time of injection. The inward propagation of Ni seems not to be hindered by the presence of the ITB: according to the SXR emission it reaches the centre in 70 ms, which reaches a maximum at 130 ms after injection, and decays with a time-constant of 300 ms. The line radiation of Ni^{24+}, Ni^{25+} and Ni^{26+} also shows fast rise and decay features. This can again only be simulated with two phases: a fast ingress phase with a strong inward convection ($V = 20 - 30\,\mathrm{m/s}$) localized outside the ITB (at $\rho \approx 0.5$), followed by a depletion phase after the ion temperature growth has come to a halt, with very low convection. A possible cause for the strong convection in the first phase is a high inward radial electric field. A similar analysis of another discharge, with a steeper pressure gradient confirm both the strong convection and the electric field as a possible cause [55]. The absence of the in-out asymmetry in these cases may be due to the peakedness of the ion density profiles [53].

5. SXR EMISSION DURING ELMS

Edge-localized modes (ELMs) are brief (≈ 0.1 ms) instabilities occurring at the edge of the plasma [56]. The case shown here is a so-called "giant" ELM, in which up to 10% of the plasma energy may be lost. During ELMs bursts of SXR radiation are often observed from the divertor region, from which under normal circumstances no SXR radiation would be expected due to the low temperatures ($T_e < 100\,\mathrm{eV}$). Because during the ELM the SXR system sees spikes on a number of channels, it is possible to derive the location from which these bursts originate from the raw measurements [57]. Tomographic reconstructions confirm this interpretation, and also give quantitative information on a second effect seen in the bulk plasma.

Tomographic reconstructions of peaked phenomena are extremely difficult. In this case they were only possible due to the relatively high spatial and temporal resolution of the SXR system and several features of the tomography algorithm. It was essential to use the non-negativity constraint because otherwise the reconstructed profile overshoots to negative values close to the peaks and large artefacts appear all over the reconstruction region. Furthermore, some artefacts were reduced by setting further constraints to the values in the grid points where these artefacts occurred. It was also important to take into account the full geometric matrix of the system, because when the measurements are interpreted as pure line integrals they are inconsistent (due to the beam widths the smallness of the peaks cannot possibly be established). For the reconstruction shown, the grid size in the divertor region was chosen smaller (2/3 the distance

between grid points) than in the main plasma to support steeper gradients. Furthermore, it was important to choose the values of $D_{\perp}$ and $D_{//}$ in the divertor region small to reduce the imposed smoothness in the divertor; they were chosen a factor of ten smaller than in the bulk (retaining their ratio). Under these conditions the matrix F to enhance the peaks had only a limited effect. The resulting tomographic reconstruction of one time slice is shown in Fig. 9.

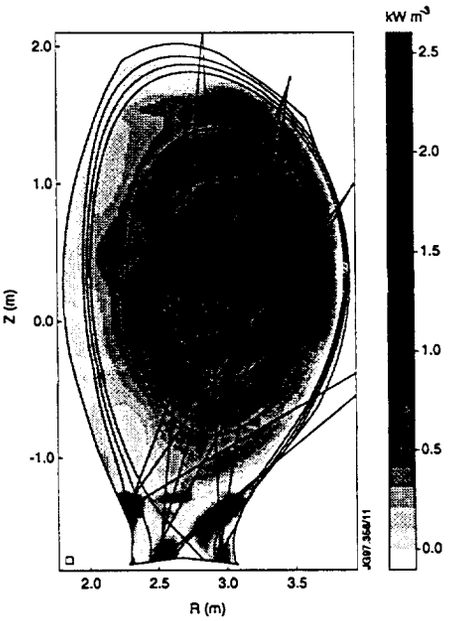

FIG. 9 Tomographic reconstruction of the SXR emission during an ELM (JET discharge 34425 at t = 17.187620 s). The same conventions as in Fig. 4 have been used, with the exceptions that the square indicates the grid size in the divertor (2/3 of the distance between grid points in the bulk) and the dashed lines indicate two flux surfaces inside the separatrix, the separatrix, and two flux surfaces in the scrape-off-layer. The solid lines indicate the lines of sight that see a peak during the ELM.

Although Fig. 9 shows some artefacts occurring along lines of sight that see the peaks in the divertor, the main features are very clear: a number of peaks in the divertor and an emitting shape in the upper-right corner of the main plasma. Two of the peaks on the inner side of the divertor clearly originate from the divertor wall. This should also be the case on the outer side of the divertor (as is found from analysis in other discharges [57]), but there are no horizontal lines of sight in the outer corner of the divertor, which means that the tomography algorithm cannot distinguish between these two solutions. These peaks can be explained as follows [57]: fast electrons created during the ELM are lost from the plasma, follow field lines in the scrape-off-layer and collide with the wall. This explains the location: outside the strike points and on the shoulders of the divertor. The high-energy electrons are slowed down in the C divertor tiles and create bremsstrahlung. Although this is an inefficient process and the Be filters transmit only a small fraction, the observed intensities are still feasible [57]. Because of the strong filtering, the angle effects of the Be filter are larger than for plasma radiation at which the absolute calibration was carried out, which can explain the inconsistencies between lines of sight which lead to some artefacts. The other feature, the emission near the edge in the upper-right corner of the main plasma can be explained as follows [57]. The radiating region is close to points on the limiter that are closest to the separatrix. Some plasma expelled into the scrape-off layer during the ELM will interact with the limiters, and deuterium neutrals will be recycled at relatively high energies into the plasma, increasing the local density which gives rise to an enhanced SXR radiation. The observed radiation regions fluctuate strongly in amplitude during an ELM, and measurements in other toroidal locations indicate that they are toroidally asymmetric.

6. DISCUSSION

The SXR tomography diagnostic on JET, with six virtually full views of the plasma, makes it possible to study many phenomena in detail. The successful application of a tomographic reconstruction algorithm incorporating several important features has been demonstrated. These features include anisotropic smoothness, reduction of smoothness near expected peaks, a non-negativity constraint, taking into account beam widths, and a variable grid size. This algorithm has made it possible to study in detail transport processes of injected trace impurities, basis functions which give a continuous solution, and the very localized SXR emission during ELMs. An error analysis on the tomographic reconstructions shows that, although the uncertainties become larger towards the centre of the plasma, even hollow profiles can be reconstructed reliably. The tomographic reconstructions are in agreement with electron density and temperature measurements within the uncertainties of each of the diagnostics.

The impurity injection experiments in hot-ion H mode plasmas indicate that an ELM instability is followed by a short-lived (~10 ms) phase of high transport, suggesting the presence of strong diffusion for the injected impurities in the outer regions of the discharge. The following quiescent phase is characterized by very low, but higher than neoclassical (by a factor 2 to 10), diffusion. In optimized-shear discharges a strong inward convection of Ni is observed, so that the Ni reaches the centre within 70 ms. Strong poloidal asymmetries due to toroidal plasma rotation are observed in the hot-ion H mode plasma, but not in the optimized-shear plasmas.

During ELMs localized fluctuating sources of SXR emission are observed on the outer edge of the bulk plasma and from the wall in the divertor. This means that energetic plasma particles expelled during an ELM spread out over areas where it was not expected.

The damage to the detectors caused by neutrons produced in DD fusion reactions is severe. Nevertheless, the measurements can be successfully interpreted after a cross-calibration method, based on tomographic reconstructions, is applied, i.e. no external calibration source is required. However, the damage limits the confidence with which the spatial structure of small phenomena, such as MHD oscillations, can be interpreted. Although specialized tomographic reconstruction techniques are applied successfully at JET for this type of phenomenon [28], it may also be possible to filter out the stationary artefacts by, for example, singular value decomposition [27,58].

ACKNOWLEDGEMENTS

The authors would like to thank JET Task Forces H and P for including the impurity injection experiments in their programmes. Furthermore, Dr. G.T.A. Huijsmans is thanked for useful discussions on basis functions.

APPENDIX A: BASIS FUNCTIONS

We define an inner product between functions $q(x,y)$ and $r(x,y)$ as (using Dirac notation)

$$\langle q|r\rangle = \iint q(x,y)\, r(x,y)\, w(x,y)\,\mathrm{d}x\,\mathrm{d}y\,,$$

where $w(x,y)$ is a weighting function. Given orthonormal basis functions b_j, as usual orthonormality requires $\langle b_i|b_j\rangle = \delta_{ij}$. The coefficients g_j in Eq. (3) are related to $g(x,y)$ by

$$g_j = \langle g|b_j\rangle.$$

A common discretization of $\boldsymbol{g}$ is into pixels of a grid (see for example Ref. 35). In this case the basis functions b are

$$b_j(x,y) = \begin{cases} 1 & \text{if } (x,y) \text{ inside the } j\text{th pixel,} \\ 0 & \text{otherwise.} \end{cases}$$

This is an example of *local* basis functions. We use local basis functions that describe bilinear interpolation between the grid points, which are pyramid shaped with rounded corners between grid points. These basis functions can be expressed as

$$b_j(x,y) = t_x(x,x_j)\, t_y(y,y_j)\,,$$

where the triangle functions t_x and t_y are given by

$$t_z(z,z_c) = \begin{cases} 0 & \text{if } z < z_c - \Delta z, \\ \dfrac{z - z_c + \Delta z}{\Delta z} & \text{if } z_c - \Delta z \le z < z_c\,, \\ \dfrac{z_c + \Delta z - z}{\Delta z} & \text{if } z_c \le z < z_c + \Delta z, \\ 0 & \text{if } z \ge z_c + \Delta z, \end{cases}$$

where z is x or y and Δz indicates the distance between grid points. These basis functions ensure that the resulting $g(x,y)$ in Eq. (3) is continuous. In the case of pixels g_j corresponds to the average emissivity in the pixel [$w(x,y) = 1$]. In the case of the bilinear interpolation, g_j corresponds to the actual value in the grid point [$w(x,y) = \Sigma_k \delta(x - x_k)\delta(y - y_k)$ and thus $g_j = g(x_j, y_j)$, (x_j, y_j) being the coordinates of grid point j].

Global basis functions, i.e. where the functions b cover the entire reconstruction area (i.e. are nonzero over a large area), can be used in the same way. An example is the expansion where

the components of $\boldsymbol{g}$ are parameters of a profile model or the coefficients of a fit given by the global orthonormal basis functions. In systems with regular coverage it is possible to find "natural" basis functions based on $K_i(x,y)$ [59]. Non-orthogonal basis functions can also be used. The non-orthogonal basis functions must be such that the coefficients g_j can be uniquely determined from Eq. (3), which is true by definition for orthogonal functions. For a comparison of various orthogonal and non-orthogonal local basis functions, see Ref. 60.

APPENDIX B: ANALYTICAL INVERSE OF EQ. (12)

We require that a solution exists and that $\ker(B) \cap \ker(C) = \{0\}$, i.e. the subspace of solution space that goes unnoticed by the experiment [$\ker(C)$] does not overlap with the subspace towards which the *a priori* information is indifferent [$\ker(B)$]. For a positive definite matrix B, the inverse of the matrix in Eq. (12) can be written as

$$[B+\lambda C]^{-1} = B^{-\frac{1}{2}}\left[I_J + \lambda B^{-\frac{1}{2}} C B^{-\frac{1}{2}}\right]^{-1} B^{-\frac{1}{2}}, \tag{B1}$$

where I_J is the unity matrix of dimension J and by definition $B^{\frac{1}{2}}B^{\frac{1}{2}} = B$. Defining the generalized eigenvalue problem

$$C|y_k\rangle = \mu_k B|y_k\rangle, \tag{B2}$$

and $|y_k\rangle = B^{-\frac{1}{2}}|u_k\rangle$, where $|u_k\rangle$ are the eigenvectors of $B^{-\frac{1}{2}} C B^{-\frac{1}{2}}|u_k\rangle = \mu_k|u_k\rangle$, it is possible to show that

$$\left[I_J + \lambda B^{-\frac{1}{2}} C B^{-\frac{1}{2}}\right]^{-1} = \sum_{k=1}^{J} \frac{|u_k\rangle\langle u_k|}{1+\lambda\mu_k},$$

which with Eq. (B1) leads to Eq. (13). To obtain the solution Eq. (13) it is therefore necessary to solve the generalized eigenvalue problem Eq. (B2) numerically. A detailed proof of the above and the general case of the matrix B not being positive definite can be found in Fehmers [43].

APPENDIX C: MINIMUM SMOOTHNESS AND DIFFUSION AS OBJECT FUNCTION

A usual functional to quantify the "total" unsmoothness and other properties of the function g, which can be expressed by a scalar product, is [27,33,40,42]

$$\langle g|\Omega|g\rangle = \iint [c_0 g^2(x,y) + c_x\left(\frac{\partial g}{\partial x}\right)^2 + c_y\left(\frac{\partial g}{\partial y}\right)^2 + c_{xx}\left(\frac{\partial^2 g}{\partial x^2}\right)^2 + 2c_{xy}\left(\frac{\partial^2 g}{\partial x \partial y}\right)^2 + c_{yy}\left(\frac{\partial^2 g}{\partial y^2}\right)^2]\,dx\,dy, \tag{C1}$$

where the integrals are over the reconstruction region. The parameters c can be chosen to suit the particular problem and can be chosen differently for different directions, i.e. leading to anisotropic smoothness. The c_0 term penalizes large values of g, for example outside the plasma. The first derivative terms force the solution to be as flat as possible (used in, for example, Ref. 27), whereas the second derivative terms force it to be smooth. Often only the second derivative terms are used because one is searching for the smoothest function. The Cartesian coordinate system used in Eq. (C1) only serves as an example: of course any coordinate system can be used in the definition of Ω by a scalar product. The coordinate system can be chosen to suit the particular problem, see for instance Ref. 61. The functional of Eq. (C1) can be written in matrix form to give

$$\Omega = \left(c_x D_x^{\mathsf{T}} D_x + c_y D_y^{\mathsf{T}} D_y + c_{xx} D_{xx}^{\mathsf{T}} D_{xx} + 2c_{xy} D_{xy}^{\mathsf{T}} D_{xy} + c_{yy} D_{yy}^{\mathsf{T}} D_{yy}\right)\Delta x \Delta y,$$

where the D designate various first and second derivative matrices [47], and Δx and Δy are the distances between grid points in the x and y directions.

The diffusion object function of Eq. (15) in Cartesian coordinates can be written very similarly to Eq. (C1):

$$\iint \left[c_x\left(\frac{\partial g}{\partial x}\right) + c_y\left(\frac{\partial g}{\partial y}\right) + c_{xx}\left(\frac{\partial^2 g}{\partial x^2}\right) + 2c_{xy}\left(\frac{\partial^2 g}{\partial x \partial y}\right) + c_{yy}\left(\frac{\partial^2 g}{\partial y^2}\right)\right]^2 dx\,dy, \tag{C2}$$

where the coefficients c are complicated, but well-defined, functions of the diffusion coefficients, the flux function, and their derivatives. Note that they are functions of x and y because the diffusion tensor and the flux are functions of the position.c_x c_y Note also that the square is taken of all terms, an not of each term separately as in Eq. (C1). In matrix form Eq. (C2) leads to Eq. (16).

The fact that some numerical derivatives on a coarse grid can be inaccurate, especially if either $\boldsymbol{n}$ and $\boldsymbol{t}$ are almost parallel to the Cartesian axes, does not cause any problems in the practical implementation: the object function is an integral over the entire grid, so numerical errors are averaged out. The coefficients c_x and c_y are singular where the derivative of the magnetic flux is zero, i.e. close to the magnetic axis. This causes numerical problems and an unrealistically high object function if the peak of the emission profile is not exactly on the magnetic axis. Therefore, a cut-off is assumed for too large c_x and c_y.

REFERENCES

[1] DUBOIS, M.A., MARTY, D.A., POCHELON, A., Nucl. Fusion **20** (1980) 1355

[2] SAUTHOFF, N.R., MCGUIRE, K.M., VON GOELER, S., Rev. Sci. Instrum. **57** (1986) 2139

[3] SMEULDERS, P., Nucl. Fusion **23** (1983) 529

[4] NAGAYAMA, Y., TSUJI, S., KAWAHATA, K., NODA, N., TANAHASHI, S., Jpn. J. Appl. Phys. **20** (1981) L779

[5] SMEULDERS, P., *A fast plasma tomography routine with second-order accuracy and compensation for spatial resolution*, Report IPP2/252 (Max-Planck-Institut für Plasmaphysik, Garching, 1983)

[6] CAMACHO, J.F., GRANETZ, R.S., Rev. Sci. Instrum. **57** (1986) 417

[7] GRANETZ, R.S., SMEULDERS, P., Nucl. Fussion **28** (1988) 457

[8] DECOSTE, R., Rev. Sci. Instrum. **56** (1985) 806

[9] GRANETZ, R.S., WANG, L., "Design of the x-ray tomography system on Alcator C-MOD," in ISPP-9, *Diagnostics for Contemporary Fusion Experiments*, ed. STOTT, P.E., *et al.* (SIP, Bologna, 1991)

[10] DA CRUZ, D.F., DONNÉ, A.J.H., Rev. Sci. Instrum. **65** (1994) 2295

[11] ALPER, B., *et al.*, Rev. Sci. Instrum **68** (1997) 778

[12] ANTON, M., DUTCH, M.J., WEISEN, H., Rev. Sci. Instrum. **66** (1995) 3762

[13] BESSENRODT-WEBERPALS, M., FUCHS, J.C., SOKOLL, M., THE ASDEX UPGRADE TEAM, *Soft x-ray diagnostics for ASDEX Upgrade*, Report IPP1/290 (Max-Planck-Institut für Plasmaphysik, Garching, 1995)

[14] EDWARDS, A.W., *et al.*, Phys. Rev. Lett. **57** (1986) 210

[15] NAGAYAMA, Y., *et al.*, Phys. Rev. Lett. **67** (1991) 3527

[16] TANZI, C.P., DE BLANK, H.J., Phys. Plasmas **4** (1997) 696

[17] BÜCHSE, R., CAMPBELL, D.J., EDWARDS, A.W., GILL, R.D., in *Proceedings of the 1992 International Conference on Plasma Physics*, Innbruck, 29 June – 3 July 1992, Ed. FREYSINGER, W., *et al.*, Europhysics Conference Abstracts Vol. 16C (EPS, 1992), Part I, pp. 375

[18] HUGON, H., *et al.*, Nucl. Fusion **32** (1992) 33
[19] PASINI, D., *et al.*, Nucl. Fusion **30** (1990) 2049
[20] GIANNELLA, R., *et al.*, Nucl. Fusion **34** (1994) 1185
[21] PASINI, D., *et al*, Plasma Phys. Control. Fusion **34** (1992) 677
[22] FUCHS, G., MIURA, Y., MORI, M., Plasma Phys. Control. Fusion **36** (1994) 307
[23] HERMAN, G.T., *Image reconstruction from projections* (Academic Press, New York, 1980)
[24] NAVARRO, A.P., OCHANDO, M.A., WELLER, A., IEEE Trans. Plasma Sci. **19** (1991) 569
[25] IWAMA, N., TAKAMI, H., TAKAMURA, S., TSUKISHIMA, T., IEEE Trans. Plasma Sci. **PS-15** (1987) 609
[26] ERTL, K., VON DER LINDEN, W., DOSE, V., WELLER, A., Nucl. Fusion **36** (1996) 1477
[27] ANTON, M., *et al.*, Plasma Phys. Control. Fusion **38** (1996) 1849
[28] HUYSMANS, G.T.A., *et al.*, in *Proceedings of the 24th EPS Conference on Controlled Fusion and Plasma Physics*, Berchtesgaden, 9–13 June 1997, Ed. Schittenhelm, M., *et al.*, Europhysics Conference Abstracts Vol. 21A (EPS, 1997), Part I, pp. 21
[29] SOKOLL M., BESSENRODT-WEBERPALS, M., ASDEX UPGRATE TEAM, in *Proceedings of the 24th EPS Conference on Controlled Fusion and Plasma Physics*, Berchtesgaden, 9–13 June 1997, Ed. Schittenhelm, M., *et al.*, Europhysics Conference Abstracts Vol. 21A (EPS, 1997), Part IV, pp. 1517
[30] FUCHS, J.C., MAST, K.F., HERMANN, A., LACKNER, K., in *Proceedings of the 21st EPS Conference on Controlled Fusion and Plasma Physics*, Montpellier, 27 June – 1 July 1994, Ed. JOFFRIN, E., *et al.*, Europhysics Conference Abstracts Vol. 18B (EPS, 1994), Part III, pp. 1308
[31] INGESSON, L.C., *et al.*, in *Proceedings of the 24th EPS Conference on Controlled Fusion and Plasma Physics*, Berchtesgaden, 9–13 June 1997, Ed. Schittenhelm, M., *et al.*, Europhysics Conference Abstracts Vol. 21A (EPS, 1997), Part I, pp. 113
[32] NATTERER, F., *The mathematics of computerized tomography* (Wiley and Teubner, Stuttgart, 1986)
[33] TURCHIN, V.F., KOZLOV, V.P., MALKEVICH, M.S., Sov. Phys. Usp. **13** (1971) 681 [Usp. Fiz. Nauk **102** (1970) 345]
[34] LEWITT, R.M., Proc. IEEE **71** (1983) 390
[35] CENSOR, Y., Proc IEEE **71** (1983) 409
[36] INGESSON, L.C., PICKALOV, V.V., J. Phys. D: Appl. Phys. **29** (1996) 3009
[37] HOWARD, J., J. Opt. Soc. Am. A **5** (1988) 999
[38] INGESSON, L.C., BÖCKER, P.J., REICHLE, R., SMEULDERS., P., "Projection-space methods to take into account finite beam-width effects in two-dimensional tomography systems," submitted to J. Opt. Soc. Am. A

[39] TAKAMURA, S., ODA, Y., SAKURAI, S., in *Proceedings of the 1992 International Conference on Plasma Physics*, Innbruck, 29 June – 3 July 1992, Ed. FREYSINGER, W., *et al.*, Europhysics Conference Abstracts Vol. 16C (EPS, 1992), Part II, pp. 859

[40] WILLIAMSON, J.H., EVANS, D.E., IEEE Trans. Plasma Sci. **PS-10** (1982) 82

[41] IWAMA, N., *et al.*, Appl. Phys. Lett. **54** (1989) 502

[42] SALAKOV, M.KH., GRACHEV, I.D., LATIPOV, R.Z., FISHMAN, I.S., Computer Enhanced Spectroscopy (USSR) **2** (1984) 117

[43] FEHMERS, G.C., *Tomography of the ionosphere*, Thesis (Technische Universiteit Eindhoven, The Netherlands, 1996)

[44] HOLLAND, A., NAVRATIL, G.A., Rev. Sci. Instrum. **57** (1986) 1557

[45] BORRÁS, M.C., GRANETZ, R.S., Plasma Phys. Control. Fusion **38** (1996) 289

[46] NAG Library Mark 16, Numerical Algorithms Group Ltd., Oxford, UK

[47] TWOMEY, S., *Introduction to the mathematics of inversion in remote sensing and indirect measurements* (Elsevier, Amsterdam, 1977)

[48] GIANNELLA, R., LAURO-TARONI, L., in *Proceedings of the 21st EPS Conference on Controlled Fusion and Plasma Physics*, Montpellier, 27 June – 1 July 1994, Ed. JOFFRIN, E., *et al.*, Europhysics Conference Abstracts Vol. 18B (EPS, 1994), Part III, pp. 1260

[49] GALLI, P., *et al.*, "Transient heat transport studies using laser ablated impurity injection in JET," submitted to Nucl. Fusion

[50] SMEULDERS, P., Nucl. Fusion **26** (1986) 267

[51] GIANNELLA, R., *et al.*, in *Proceedings of the 1992 International Conference on Plasma Physics*, Innsbruck, 29 June – 3 July 1992, Ed. FREYSINGER, W., *et al.*, Europhysics Conference Abstracts Vol. 16C (EPS, 1992), Part I, pp. 279

[52] WESSON, J.A., Nucl. Fusion **37** (1997) 577

[53] ROMANELLI, M., *et al.*, in *Proceedings of the 24th EPS Conference on Controlled Fusion and Plasma Physics*, Berchtesgaden, 9–13 June 1997, Ed. Schittenhelm, M., *et al.*, Europhysics Conference Abstracts Vol. 21A (EPS, 1997), Part I, pp. 5

[54] THE JET TEAM (presented by SÖLDNER, F.X.), Plasma Phys. Control. Fusion **39**, suppl. 12B (1997) B353

[55] GIANNELLA, R., *et al.*, in *Proceedings of the 24th EPS Conference on Controlled Fusion and Plasma Physics*, Berchtesgaden, 9–13 June 1997, Ed. Schittenhelm, M., *et al.*, Europhysics Conference Abstracts Vol. 21A (EPS, 1997), Part I, pp. 53

[56] ZOHM, H., Plasma Phys. Control. Fusion **38** (1996) 105

[57] GILL, R.D., *et al.*, "Particle and energy flow following giant ELMs in JET," to be published

[58] FURNO, I., *et al.*, "X-ray measurements of MHD activity in shaped TCV plasmas", to appear in *Proceedings of the 24th EPS Conference on Controlled Fusion and Plasma Physics*, Berchtesgaden, 9–13 June 1997

[59] BUONOCORE, M.H., BRODY, W.R., MACOVSKI, A., IEEE Trans. Biomedical Engineering **BME-28** (1981) 69
[60] HANSON, K.M., WECKSUNG, G.W., Appl. Opt. **24** (1985) 4028
[61] MLYNÁR, J., Czech. J. Phys. **45** (1995) 799